The Astrophysical Journal Supplement Series, 253:44 (16pp), 2021 April https://doi.org/10.3847/1538-4365/abe469

SiO, ^{29}SiO, and ^{30}SiO Emission from 67 Oxygen-rich Stars: A Survey of 61 Maser Lines from 7 to 1 mm

J. R. Rizzo[1,2], J. Cernicharo[3], and C. García-Miró[4]
[1] Centro de Astrobiología (INTA-CSIC), Ctra. M-108, km. 4, E-28850 Torrejón de Ardoz, Madrid, Spain; ricardo.rizzo@cab.inta-csic.es
[2] ISDEFE, Beatriz de Bobadilla 3, E-28040 Madrid, Spain
[3] Grupo de Astrofísica Molecular, Instituto de Física Fundamental (IFF-CSIC), C/ Serrano 121, E-28006 Madrid, Spain
[4] Joint Institute for VLBI ERIC (JIVE), Oude Hoogeveensedijk 4, 7991 PD Dwingeloo, The Netherlands
Received 2020 November 2; revised 2021 January 28; accepted 2021 February 1; published 2021 March 26

Abstract

Circumstellar environments of oxygen-rich stars are among the strongest SiO maser emitters. Physical processes such as collisions, infrared pumping, and overlaps favor the inversion of level population and produce maser emission at different vibrational states. Despite numerous observational and theoretical efforts, we still do not have a unified picture including all of the physical processes involved in SiO maser emission. The aim of this work is to provide homogeneous data in a large sample of oxygen-rich stars. We present a survey of 67 oxygen-rich stars from 7 to 1 mm, in their rotational transitions from $J = 1 \rightarrow 0$ to $J = 5 \rightarrow 4$, for vibrational numbers v from 0 to 6 in the three main SiO isotopologs. We have used one of the 34 m NASA antennas at Robledo and the IRAM 30 m radio telescope. The first tentative detection of a $v = 6$ line is reported, as well as the detection of new maser lines. The highest vibrational levels seem confined to small volumes, presumably close to the stars. The $J = 1 \rightarrow 0$, $v = 2$ line flux is greater than the corresponding $v = 1$ in almost half of the sample, which may confirm a predicted dependence on the pulsation cycle. This database is potentially useful in models which should consider most of the physical agents, time dependency, and mass-loss rates. As a by-product, we report detections of 27 thermal rotational lines from other molecules, including isotopologs of SiS, H_2S, SO, SO_2, and NaCl.

Unified Astronomy Thesaurus concepts: Silicon monoxide masers (1458); Asymptotic giant branch (108); Interstellar medium (847); Interstellar molecules (849); Circumstellar envelopes (237); Stellar evolution (1599); Surveys (1671); Radio astronomy (1338)

Supporting material: data behind figure, machine-readable tables

1. Introduction

Evolved oxygen-rich stars are among the most powerful maser emitters known to date. Maser emission in ^{28}SiO rotational transitions of vibrationally excited states is ubiquitous and very intense in these sources. Rotational transitions up to $J = 7 \rightarrow 6$ have been detected in the vibrational states $v = 1$, 2, 3, and 4 (Jewell et al. 1987; Cernicharo et al. 1993; Gray et al. 1995, and references therein). A certain number of maser lines have been also detected in the ground and excited vibrational states of the rare isotopologs ^{29}SiO and ^{30}SiO (e.g., Deguchi et al. 1983; Cernicharo et al. 1991; Alcolea & Bujarrabal 1992; Cernicharo & Bujarrabal 1992; González-Alfonso et al. 1996).

Despite the large amount of observational data available in the literature, SiO maser emission has complex aspects that deserve further observational and theoretical effort. Besides the overall inversion of the rotational levels in each vibrational ladder, the SiO emission displays intriguing anomalies in some specific rotational lines, such as drastic changes in intensity from one rotational line to the next within the same v state. Although the general inversion process seems to be relatively well understood (e.g., Bujarrabal 1994a, 1994b), the differences in the emission of adjacent rotational lines are difficult to explain using standard radiative and collisional pumping models.

Such anomalies, which are particularly important for the high-v states of ^{28}SiO, also apply to the less-abundant isotopologs ^{29}SiO and ^{30}SiO in $v = 0$, 1, 2, and 3 (Cernicharo et al. 1991, 1993; Cernicharo & Bujarrabal 1992). They have been interpreted as a result of infrared overlaps between the rovibrational lines of ^{28}SiO, ^{29}SiO, and ^{30}SiO (González-Alfonso & Cernicharo 1997; Herpin & Baudry 2000). The excitation of the vibrational levels depends on the amount of dust in the envelope and on the effective temperature of the star photosphere. Furthermore, an overlap between SiO and H_2O has been proposed to explain the $v = 2$ $J = 2 \rightarrow 1$ line of ^{28}SiO (Olofsson et al. 1981, 1985; Langer & Watson 1984; Bujarrabal et al. 1996).

Optical pumping is also a possible mechanism to account for the observed features in these lines. Rausch et al. (1996) have modeled synthetic atmospheres of M stars immersed in expanding envelopes and showed that optical pumping may account for some features of maser emission even without collisions; moreover, the regions of inversion may be different from one isotopolog to another, depending on the velocity difference between the photosphere and the emitting volume. Optical pumping through the $A^1\Pi - X^1\Sigma$ electronic transition could be very efficient in stars with moderate/low mass-loss rate and hot photospheres in which photons at 250 nm could excite the $^1\Pi$ state. Excitation through the triplet states of SiO could also occur at 330 nm.

The excitation of the SiO masers through collisions with H_2 and He is still an open subject. Before the work of Dayou & Balança (2006), who performed new potential energy surface calculations of the system SiO/He/p-H_2, there were no accurate rovibrational collisional rates. Recently, Balança & Dayou (2017) extended the computation of collisional rates with He in the temperature range 300–6000 K, for the first six vibrational levels and up to the rotational states $J = 40$.

Despite the many years since the discovery of SiO masers, robust and realistic models that take into account all of the possible mechanisms for pumping are still necessary. To distinguish between the different physical processes leading to the population inversion of the SiO energy levels, and to retrieve key information about the physical conditions of the gas in the region between the photosphere and the dust growth zone, it is necessary to gather the most complete, simultaneous, and homogeneous sample of the SiO rotational emission in the different vibrational states. The current availability of wideband backends spanning several GHz of instantaneous bandwidths makes possible nowadays this kind of study. These backends permit the simultaneous observation of multiple spectral lines, avoiding the problem of intrinsic variability. Furthermore, it permits optimizing the observing time and minimizing the impact of the uncertainties of physical parameters associated with calibration and pointing.

There are dozens of SiO surveys of evolved stars, covering different lines, isotopologs, and in some cases, with great detail of the emitting regions thanks to the use of interferometers. Some of the most complete surveys include the observation of 11 lines of ^{28}SiO in 6 evolved stars by Schwartz et al. (1982), the line survey in the red supergiant VY CMa by Cernicharo et al. (1993), the study of 12 sources by Pardo et al. (1998), the survey by Cho et al. (1996) of 6 $J=1\rightarrow0$ transitions in various vibrational states of ^{28}SiO and ^{29}SiO, and the study of the $J=1\rightarrow0$ $v=1$ and 2 lines done by Kim et al. (2010). Most of the other studies, however, have been carried out in different epochs, with different instruments and, sometimes, without a complete coverage of the rotational transitions from different vibrational levels. Due to the variability of the SiO maser emission and to the complexity of the physics of stellar pulsation (which is in turn associated with the line pumping), the observations gathered in different epochs cannot be compared to infer robust conclusions about the excitation of SiO.

In this paper, we report a survey of SiO, ^{29}SiO, and ^{30}SiO maser lines toward 67 evolved oxygen-rich stars. The selected sources span different mass losses, temperatures, and C/O abundance ratios.[5] As a by-product, this work also provides valuable information about the molecular content of these objects in the surveyed frequency ranges. The survey was done using one of the 34 m antennas of the Madrid Deep Space Communications Complex (hereafter MDSCC) and the IRAM 30 m radio telescope at Pico Veleta. A total of 61 transitions from $J=1\rightarrow0$ to $5\rightarrow4$, and $v=0$ to 6 was observed in the whole sample. In Section 2, we describe the observations. We present the results in Section 3. In Section 4, we discuss some global results of the survey, including polarization, variability, some special cases, and the identification of other spectral lines. We summarize the main findings in Section 5. In a follow-up paper, we plan to use this database to model the circumstellar envelopes (CSEs), using an already developed nonlocal radiative transfer code that includes infrared overlaps between the three silicon isotopes of SiO, collisional pumping, and optical and infrared excitation.

2. Observations

2.1. Overview, Sources, and Strategy

As mentioned in the previous section, we have done a survey of 67 oxygen-rich evolved stars in their SiO, ^{29}SiO, and ^{30}SiO maser line emission. The DSS-54 antenna of the Madrid Deep Space Communications Complex (MDSCC) was used in the first part of the survey to observe the $J=1\rightarrow0$ lines, at a wavelength of 7 mm ($\sim$ 43 GHz). Based on these initial results, we observed the most relevant sources in the $J=2\rightarrow1$ to $5\rightarrow4$, at wavelengths of 3, 2, and 1 mm, using the 30 m IRAM radio telescope at Pico Veleta (Spain). The MDSCC observations were done between 2012 March and July, and the IRAM observations in 2012 August.

We have chosen the observing modes and bands in order to optimize the tuning of the largest possible number of simultaneous lines. The lines observed (61 in total) and their corresponding frequencies are indicated in Table 1. The frequencies have been obtained from the CDMS[6] (Müller et al. 2001, 2005) and the JPL[7] (Pickett et al. 1998) catalogs. We also used information from MADEX[8] (Cernicharo 2012) when the above-mentioned catalogs did not provide sufficient precision. The list of the observed sources are presented in Table 2, together with some useful information, such as the date of observation, transitions, observing modes, velocity spacing, integration time, rms noise, and polarization recorded. The DSS-54 antenna is able to record both circular polarizations, while the 30 m radio telescope records linear polarizations.

The half-power beamwidth (HPBW) of both telescopes at different frequencies are indicated in Table 3, together with sensitivities and efficiencies. The spectra have been corrected for atmospheric opacity and elevation gain (T_a^* scale) during the observation, and converted to flux density (S scale) during the reduction process. The conversion from T_a^* to main-beam temperature (T_{MB}) can be done by $T_{MB}=T_a^*/\eta_{MB}$, with η_{MB} the main-beam efficiency, also depicted in Table 3. Unless specifically stated, we use the flux density scale (in jansky) throughout the paper, and in the machine-readable tables.

2.2. MDSCC Observations

We used the NASA DSS-54 antenna of the MDSCC to observe the $J=1\rightarrow0$ lines included in the survey (Table 1). The DSS-54 is a beam–waveguide antenna 34 m in diameter. The new Q-band receiver was employed, which has a temperature of 35 K at 43 GHz (Rizzo & García-Miró 2013). The final system temperatures were between 90 and 130 K, on the antenna temperature scale.

The two circular polarizations from the receiver were processed by the new wideband backend (Rizzo et al. 2012). The observations were done in 14 different sessions between 2012 March 23 and July 26. In the beginning, the backend had the capacity to process a single circular polarization, with a bandwidth of 1.5 GHz, 8192 channels, and a frequency spacing of $\sim$183 kHz (equivalent to 1.28 km s^{-1}). At some point during the survey, a second FFTS board was incorporated, allowing the possibility of observing both circular polarizations simultaneously and using a high-resolution mode, which provided 500 MHz of bandwidth, 16384 channels, and a frequency spacing of $\sim$31 kHz (equivalent to 0.21 km s^{-1}). The broadband FFTS backend was centered at 42.75 GHz, which allowed us to simultaneously observe the 10 lines indicated in Table 1. The 500 MHz bandwidth FFTS was always centered at

[5] The C/O abundance ratio is <1 for the whole sample. Carbon stars, which have C/O > 1, exhibit SiO thermal emission but not maser lines.

[6] http://www.astro.uni-koeln.de/cgi-bin/cdmssearch

[7] http://spec.jpl.nasa.gov/ftp/pub/catalog/catform.html

[8] https://nanocosmos.iff.csic.es/madex/

Table 1
Frequencies of the Observed Lines (in MHz)

SiO					
v	$J=1\rightarrow 0$	$J=2\rightarrow 1$	$J=3\rightarrow 2$	$J=4\rightarrow 3$	$J=5\rightarrow 4$
0	43423.85163	86846.9600	130268.6100	173688.3100	217104.9800
1	43122.07310	86243.3700	129363.2400	172481.1500	215595.9500
2	42820.58624	85640.4600	128458.8872	171275.2800	214088.5400
3	42519.38333	85038.0464	127555.2739	170070.3500	212582.6000
4	42218.45653	84436.1911	126652.4901	168866.6332	211077.8700
5		83834.8731		167663.9945	
6		83234.0760		166462.3977	
^{29}SiO					
v	$J=1\rightarrow 0$	$J=2\rightarrow 1$	$J=3\rightarrow 2$	$J=4\rightarrow 3$	$J=5\rightarrow 4$
0	42879.94655	85759.1990	128637.0500	171512.8027	214385.7577
1	42583.82840	85166.9603	127748.6912	170328.3228	212905.1554
2	42287.99473	84575.2900	126861.1851	169144.9799	211425.9744
3		83984.1744		167962.7457	209948.1793
4				166781.6000	
5				165602.4900	
^{30}SiO					
v	$J=1\rightarrow 0$	$J=2\rightarrow 1$	$J=3\rightarrow 2$	$J=4\rightarrow 3$	$J=5\rightarrow 4$
0	42373.42369	84746.1702	127117.5479	169486.8766	211853.4736
1	42082.54453	84164.4095		168323.3529	210399.0665
2		83583.2041		167160.9396	
3				165999.6090	

Table 2
Sources Observed

ID	Source	R.A. (J2000) (hh:mm:ss.ss)	Decl. (J2000) (±dd:mm:ss.s)	$V_{\rm LSR}$ (km s^{-1})	Date[a] (mm-dd)	$J\rightarrow J-1$	Mode[b]	Vel. spacing (km s^{-1})	$t_{\rm int}$ (min)	rms[c] (Jy)	Pol.[d]
1	Y Cas	00:03:21.40	+55:40:52.2	−17.0	05-21	1 − 0	FSw	1.28	24	0.05	LCP
2	IRC+40004	00:06:53.24	+43:05:03.0	−19.7	05-21	1 − 0	FSw	1.28	9	0.06	LCP
3	T Cas	00:23:14.27	+55:47:33.2	1.0	05-21	1 − 0	FSw	1.28	15	0.06	LCP
4					08-01	2 − 1	WSw	0.66	16	0.14	HLP
5					08-01	2 − 1	WSw	0.66	16	0.14	VLP
6					08-03	2 − 1	WSw	0.66	30	0.12	HLP
7					08-03	2 − 1	WSw	0.66	30	0.12	VLP
8					08-03	3 − 2	WSw	0.46	15	0.14	HLP
9					08-03	3 − 2	WSw	0.46	15	0.13	VLP
10					08-01	4 − 3	WSw	0.34	8	1.20	HLP

Notes.
[a] All dates in the year 2012.
[b] PSw: position switching. FSw: frequency switching. WSw: wobbler switching.
[c] 1σ rms value.
[d] Polarizations: LCP = left circular; RCP = right circular; HLP =h orizontal linear; VLP = vertical linear.
[e] $1-0^*$ includes only the $v=1$ and 2 lines of ^{28}SiO, and the $v=0$ line of ^{29}SiO.
[f] $4-3^*$ includes the $v=4$–6 lines of ^{28}SiO, the $v=2$–5 lines of ^{29}SiO, and the $v=0$–3 lines of ^{30}SiO.

(This table is available in its entirety in machine-readable form.)

Table 3
Efficiencies and Intensity Conversions

Frequency (GHz)	HPBW ($''$)	$S/T_{\rm a}^*$ (Jy K^{-1})	$\eta_{\rm MB}$	η_a
43	48	6.41	0.57	0.46
86	29	5.89	0.81	0.63
129	19	6.28	0.76	0.57
172	14	6.80	0.70	0.54
216	11	7.52	0.62	0.49

42.97 GHz, in order to simultaneously observe the $J=1\rightarrow 0$ maser lines of SiO $v=1$, 2, and ^{29}SiO $v=0$. This setup is indicated as $1-0^*$ in Table 2.

A total of 56 stars have been observed using this telescope with the largest bandwidth (1.5 GHz), 11 of those during two or more days for cross-checking and to study possible variability. A total of 28 out of those 56 target stars have also been observed with the high-resolution mode (i.e., 500 MHz bandwidth) to increase details about the line profiles.

Table 4
Detections

ID	Source	Transition[a]	Flux (Jy km s^{-1})	Error	V_{LSR} (km s^{-1})	Error	V_{min} (km s^{-1})	V_{max}	Individual Comments
1	Y Cas	^{28}SiO(1−0)v1	47.22	0.06	−18.65	0.37	−24.6	−9.3	
		^{28}SiO(1−0)v2	50.85	0.07	−19.56	0.45	−25.3	−15.1	
		^{28}SiO(1−0)v3	24.13	0.07	−14.37	0.46	−18.9	−8.6	
3	T Cas	^{28}SiO(1−0)v1	67.42	0.08	−10.14	0.42	−15.5	−4.1	
		^{28}SiO(1−0)v2	239.76	0.08	−10.31	0.43	−15.0	−3.5	
		^{29}SiO(1−0)v0	0.65	0.23	−5.20	1.28	−5.8	−4.5	
4	T Cas	^{28}SiO(2−1)v0	2.32	0.14	−5.08	0.34	−6.4	−3.7	
		^{28}SiO(2−1)v1	253.77	0.06	−7.67	0.16	−12.8	−0.6	
		^{28}SiO(2−1)v2	59.17	0.08	−7.70	0.21	−12.2	−4.6	

Note.
[a] Transition name includes the isotopolog, the rotational transition, and the vibrational state. As an example, the transition ^{28}SiO(4−3)v2 should be interpreted as the $J = 4 \rightarrow 3$ line of the ^{28}SiO species, at the vibrational state $v = 2$.

(This table is available in its entirety in machine-readable form.)

We corrected the observed positions by assuming the standard pointing model for this antenna in the *Q* band, which is accurate to within 8″. This model was also regularly checked and improved at specific sessions in the epoch of observations, and we estimate that pointing errors can account for intensity uncertainties always below 10%. At the beginning of each observing session, we also cross-checked the pointing by means of the observation of sources included in the paper of Rizzo et al. (2012). The focus was optimized for the *Q* band using specific calibration sessions and automatically corrected during observations as part of the standard operating mode of the antenna.

Most of the observations were done in position-switching mode, with a reference located at 6′ in azimuth. In 38 cases, we observed in frequency-switching mode, with a frequency throw of 13.2 MHz to avoid ripples. The atmospheric opacity was always between 0.07 and 0.1.

2.3. IRAM Observations

We used the IRAM 30 m radio telescope in Pico Veleta, Spain, to observe the $J = 2 \rightarrow 1$ to $5 \rightarrow 4$ lines (Table 1). The observations were done between 2012 August 1 and 4. Precipitable water vapor varied between 4 and 12 mm, which resulted in opacities at 225 GHz between 0.1 and 0.7. Most of the observations were done during night time.

The EMIR (Eight MIxer Receiver; Carter et al. 2012) was used for all the observations. The focal plane geometry of this receiver allows us to gather two bands simultaneously, in two linear polarizations. We used the new FTS backend (Klein et al. 2009), which provided a total of eight units having 4 GHz of bandwidth each and a frequency spacing of ∼195 kHz. Four of these units were always used at the 3 mm band, tuned at 85.045 GHz (the central frequency of the $J = 2 \rightarrow 1$ lines) and 88.775 GHz in both polarizations. The other band (2 or 1 mm bands) was chosen according to weather conditions to ensure the best use of the observing time. Central frequencies were 128.675, 172.025, and 215.575 GHz for the $J = 3 \rightarrow 2$ to $5 \rightarrow 4$ bands. A complementary tuning at 168.290 GHz was necessary to include the $J = 4 \rightarrow 3$ lines of SiO at $v = 4$–6, ^{29}SiO at $v = 2$–5, and ^{30}SiO at $v = 0$–3; this additional mode is indicated as "4 − 3*″ in Table 2. The 3 mm unit centered at 88.775 GHz was used to search for other molecules.

The observations were done in wobbler switching mode (which provides very flat baselines), with a throw at 90″ at a rate of 2 Hz. System temperatures varied in the ranges 110–220 K, 134–360 K, 770–3080 K, and 390–1300 K for the $J = 2 \rightarrow 1$ to $5 \rightarrow 4$ bands. The spectra have been automatically corrected by atmospheric opacity during the observations using the ATM package (Pardo et al. 2001). The antenna gain elevation curve, sensitivity, and efficiencies provided in Table 3 were computed based on the observatory web pages.

Pointing was checked every 1–1.5 hr and is accurate to within 3″. Every day, we also observed W3(OH) as a line calibrator (Mauersberger et al. 1989). The focus was checked and corrected at the beginning of each session and after sunset.

A total of 38 sources have been observed, 11 of them not included in the MDSCC sample.

3. Results

3.1. Overview

All detections are presented in Table 4. In each row, the table depicts the observation ID, the source name, the transition detected, the parameters of the lines, and individual comments (if any). The transitions in each entry contain the isotopolog, the rotational quantum numbers $J \rightarrow J - 1$, and the vibrational state. The parameters include the line flux (F), the flux-weighted velocity (V_{LSR}), and the velocity range of emission above 3σ (V_{min} and V_{max}).[9] F and V_{LSR} were computed in the velocity range (V_{min}, V_{max}). Some relevant information are also added in several entries to Table 4 as individual comments. These remarks mostly refer to the cases when data smoothing has been applied to improve the signal-to-noise ratio. In other cases, information about polarization and line blending is included. The only instrumental feature that we noted lies ∼20 MHz apart from the $J = 5 \rightarrow 4$, $v = 3$ line of ^{28}SiO; although the detection and parameters are fairly well

[9] V_{min} and V_{max} were determined by the first and last occurrences of two consecutive channels with temperatures above 3σ.

Table 5
Detections after Averages

Averaged IDs	Source	Transition[a]	Flux (Jy km s^{-1})	Error (Jy km s^{-1})	V_{LSR} (km s^{-1})	Error (km s^{-1})	V_{min} (km s^{-1})	V_{max} (km s^{-1})	Individual Comments
4–7	T Cas	^{29}SiO(2−1)v0	0.35	0.14	−4.97	0.68	−5.3	−4.7	
24–25	IRC+10011	^{29}SiO(4−3)v0	2.55	0.53	9.86	0.24	9.5	10.2	
38–41	S Cas	^{29}SiO(2−1)v0	4.51	0.11	−30.98	0.77	−35.0	−20.6	Smoothed to 2.0 km s^{-1}
38–41	S Cas	^{30}SiO(2−1)v0	0.74	0.31	−37.76	2.76	−39.0	−36.2	Smoothed to 2.8 km s^{-1}
44–45	S Cas	^{28}SiO(4−3)v0	38.19	0.07	−20.06	0.03	−31.6	9.5	

Note.
[a] Transition name includes the isotopolog, the rotational transition, and the vibrational state. As an example, the transition ^{28}SiO(4−3)v2 should be interpreted as the $J = 4 \rightarrow 3$ line of the ^{28}SiO species, at the vibrational state $v = 2$.

(This table is available in its entirety in machine-readable form.)

determined, the cases in which the spurious feature is observed are commented in the table.

For some cases, improvement of the signal-to-noise ratio was necessary to achieve clear detections; this was done by the average of data gathered during different days and/or from different polarizations. These cases are shown in Table 5, in the same format as Table 4. These averaged spectra not only allowed the detection of lines, but also permitted us to identify wide components in at least two cases: the $J = 2 \rightarrow 1$ $v = 0$ line of ^{29}SiO in S Per and in the $J = 2 \rightarrow 1$ $v = 0$ line of ^{28}SiO in IRC+60154 (see comments in Table 5).

As an example, Figure 1 depicts the full-range spectrum of one of the sources (IRC+10011 = WX Psc) in the $J = 1 \rightarrow 0$ transitions. In this case, 6 over a total of 10 possible lines are detected.

3.2. Some Examples of Individual Features

In the following, a series of figures illustrates some of the properties found in the sample, particularly with respect to line shapes, variability, and polarization.

Line profiles. The physical conditions to pump masers are so restrictive that the emitting volumes are relatively small; therefore, one of the fingerprints of the maser emission is that the velocity components are narrow, typically 1 km s^{-1} or even less.

Depending on the pumping mechanisms and the physical conditions, the maser-emitting regions dramatically change from one source to another, and also from one line to another (Gray et al. 2009). This trend is confirmed by high angular resolution observations (see, for example, Soria-Ruiz et al. 2007; Wittkowski et al. 2007). When these kinds of sources are observed by single dishes, though, the different emitting regions and physical conditions are reflected in a variety of line profiles.

Figure 2 shows six representative examples of the line shapes present in the catalog. For each panel, the source name is indicated on the upper left and the transition (in abridged format) in the upper-right corner. In the case of S Per, the spectrum is dominated by two peaks, but is the result of a superposition of several individual blended components. In the case of S Cas, the shape of a truncated parabolic and wide line is indicative of thermal emission from the CSE as a whole. In O Cet, the ^{28}SiO $J = 4 \rightarrow 3$, $v = 2$ line displays a component at ∼57 km s^{-1}, which is right outside the velocity range of the thermal line; the $J = 4 \rightarrow 3$, $v = 1$ line (lower left panel) has a Gaussian shape and is centered at the star's velocity. The line depicted for IRC+10011 is representative of a typical very narrow maser line. Finally, the line displayed for NML Tau (^{30}SiO $J = 3 \rightarrow 2$, $v = 0$) seems to be the result of the superposition of both the CSE thermal component and at least one maser component.

Variability. Most of the SiO and isotopolog maser lines in evolved stars develop a high degree of variability on scales from days to years (Humphreys et al. 2002; Pardo et al. 2004). The $J = 1 \rightarrow 0$ line observations performed with the Robledo antenna have been repeated in 11 sources, taking from 2 to 5 spectra spread in time from several days to few weeks, as indicated in Table 2. Figure 3 plots all of the measured line fluxes, normalized to their respective averages. While some sources do not display large changes in any of the two lines, other sources vary significantly within the observed time frame. The standard deviation of these data is 22% and 26% for the $v = 1$ and $v = 2$ lines, respectively. The case of μ Cep is remarkable, presenting a dramatic variation where the highest fluxes are roughly double the lowest ones. In order to provide more details, Figure 4 shows all of the observed spectra, gathered during three different days and in both circular polarizations. The emission is not significantly polarized, as we may infer from the second and third columns. It is evident in the figure that the line fluxes experienced a sudden increase in the last day, just some weeks after a rather stable maser emission; more interestingly, the changes are found in totally different velocity components for the $v = 1$ and $v = 2$ lines.

Another clear example of line variability is shown in Figure 5, where the ^{30}SiO $J = 1 \rightarrow 0$, $v = 0$ line of VX Sgr significantly changed in just two weeks.

Polarization. A significant part of the maser lines are often linearly and circularly polarized due to intrinsic magnetic fields (e.g., Shinnaga et al. 2004; Vlemmings et al. 2011; Shinnaga et al. 2017). The IRAM spectra contain valuable information about the linear polarization of these sources, although it is not possible to derive the Stokes parameters with the present observations, even though the simultaneous observations of both linear polarizations during four consecutive nights allowed the discovery of highly polarized components. Two examples are shown in Figure 6: in IRC+10011, the ^{30}SiO $J = 2 \rightarrow 1$ $v = 0$ line depicts in the horizontal polarization a component at ∼10 km s^{-1}), which is virtually absent in the vertical polarization; the second example is VY CMa, where the SiO $J = 4 \rightarrow 3$ $v = 3$ line displays significant differences

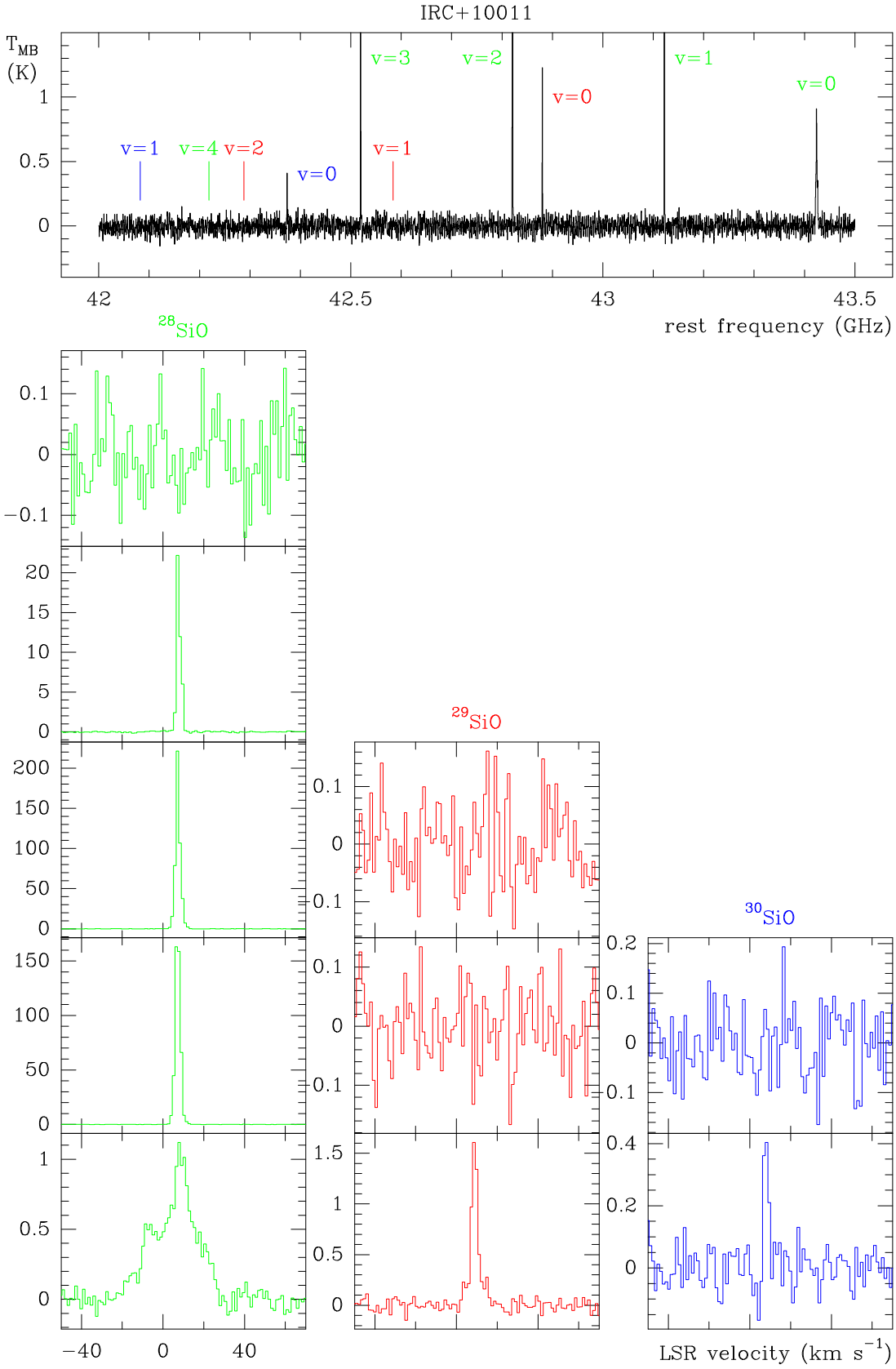

Figure 1. A full-range spectrum, aiming to show the complexity of the lines. This example corresponds to the source IRC+10011, in the $J = 1 \rightarrow 0$ lines. The upper panel shows the whole spectrum, while the lower, small panels display individual lines. Green, red, and blue correspond to ^{28}SiO, ^{29}SiO, and ^{30}SiO, respectively. For each isotopolog, vibrational number v increases from bottom to top, starting at zero. In this example, 6 out of 10 possible lines were detected. All the observed spectra, as indicated in Table 2, are available online.

(The data used to create this figure are available.)

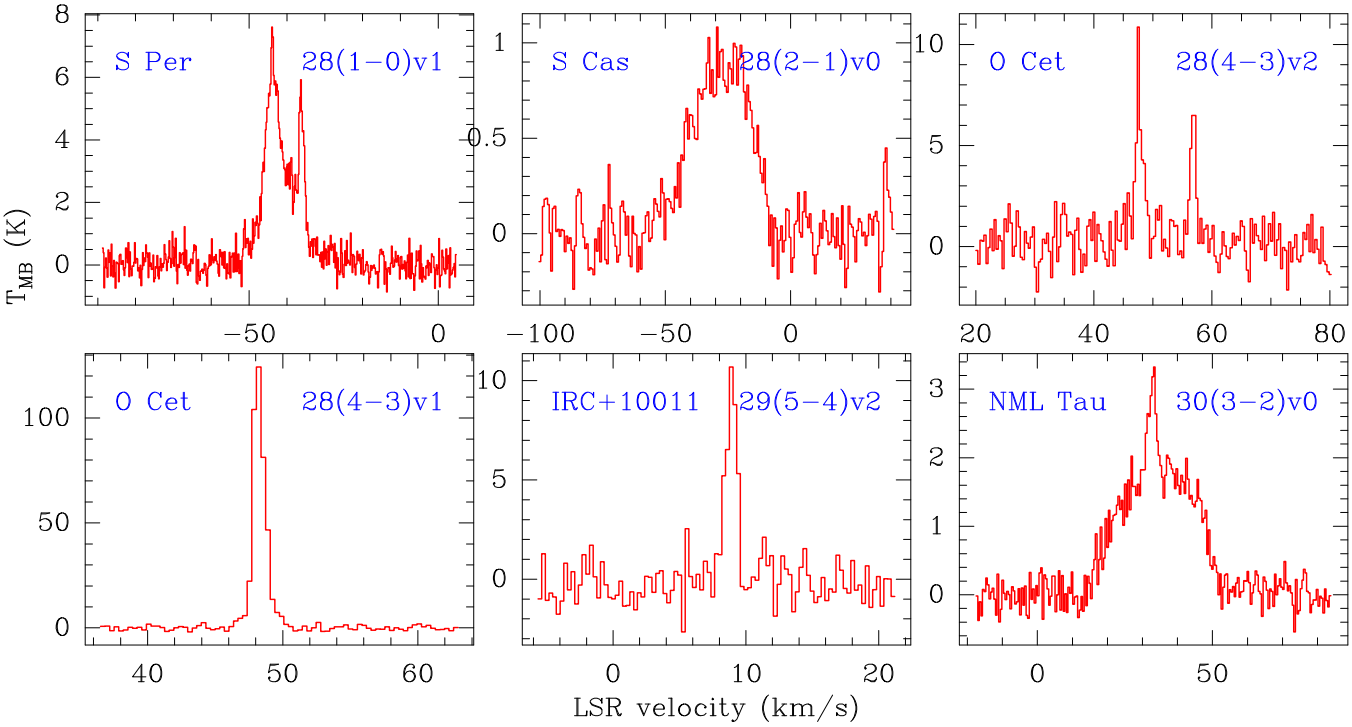

Figure 2. A sample of six different line profiles, representative of the catalog. Source names are indicated at the upper-left corner of each panel, while the lines (abridged) are shown in the upper-right corner.

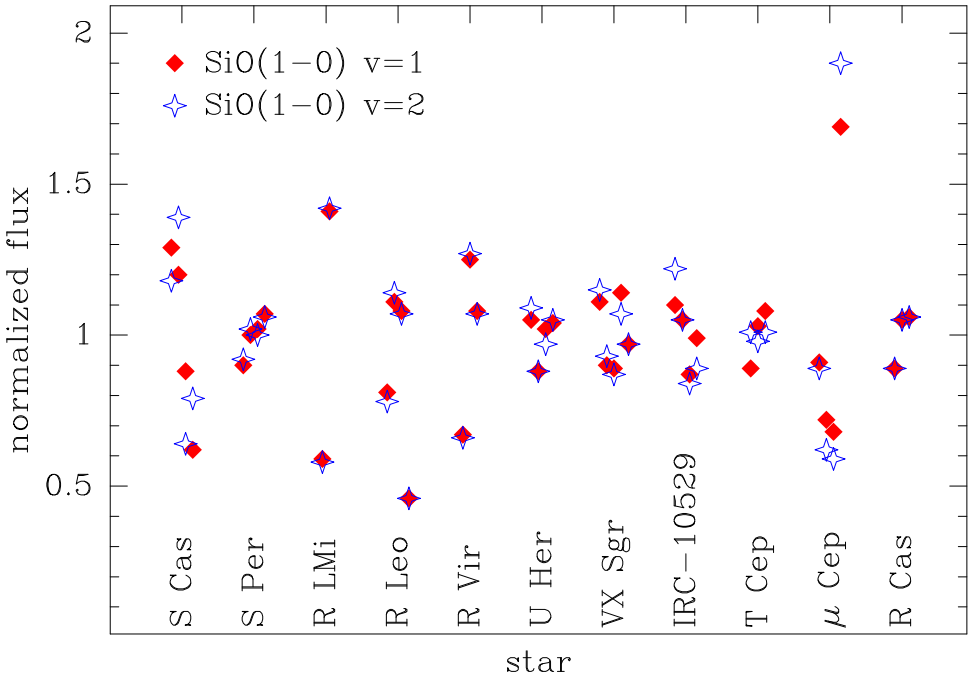

Figure 3. Variability of the $J = 1 \rightarrow 0$, $v = 1$, and $v = 2$ line fluxes corresponding to the 11 stars observed on 2 or more different days. Fluxes are normalized to their respective averages. Red and blue marks represent fluxes corresponding to the $v = 1$ and $v = 2$ lines, respectively. In most cases, the variability is clearly noted on timescales of several days to few weeks. The variability of μ Cep is remarkable, where the highest fluxes in both lines are almost twice the other values (see text and Figure 4).

between the two linear polarizations in the two principal velocity components.

3.3. Identification of Other Spectral Lines

For a significant fraction of the sample, a frequency range of up to ≈30 GHz has been surveyed. This large bandwidth also permits the search for other molecules. For each source, we averaged the spectra corresponding to all dates and polarizations, and looked for molecular species other than SiO and its isotopologs.

A total of 27 lines have been detected. Table 6 provides the list of those spectral lines together with some useful information, such as the frequencies, quantum numbers, and

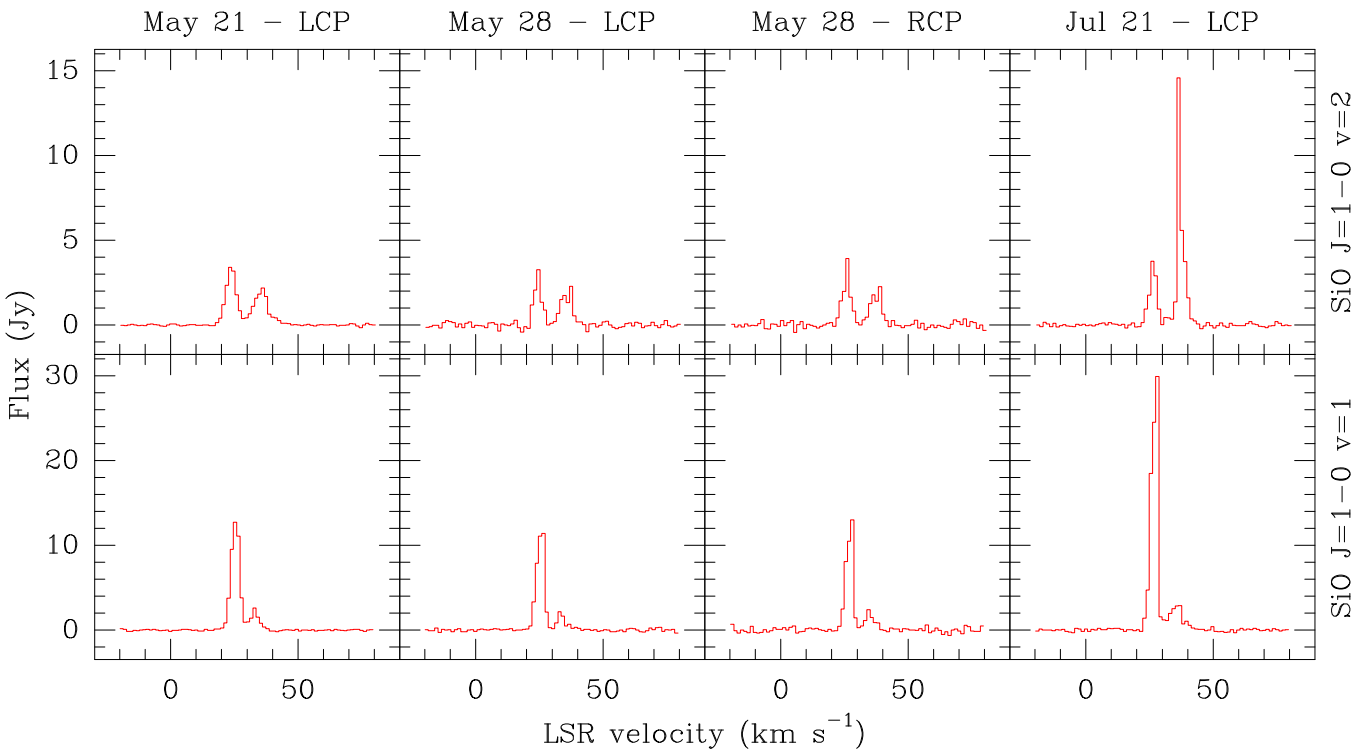

Figure 4. Variability of μ Cep. Lower and upper rows correspond to the $J = 1 \rightarrow 0$, $v = 1$, and $v = 2$ lines, respectively. Observation dates and circular polarizations are indicated on top. The emission does not seem significantly polarized (second and third columns). The notable increment experienced in the last day (fourth column) arises from the different velocity components in the two maser lines.

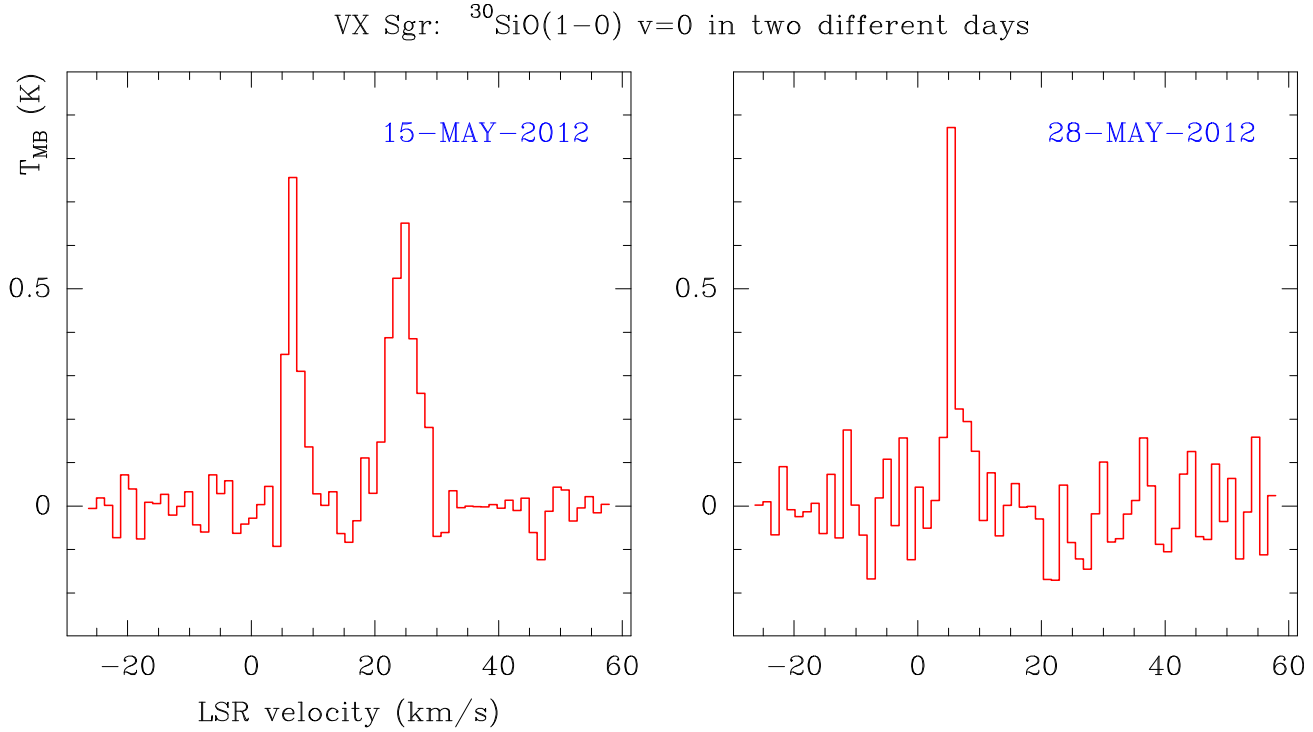

Figure 5. An example of variability. The ^{30}SiO $J = 1 \rightarrow 0$, $v = 0$ line of VX Sgr has been observed two times, with a time separation of only two weeks, but resulting in very different spectra.

energies of the upper levels. For the sake of brevity, we labeled the spectral lines by a letter followed by a number; the letter indicates the molecular species, while the number designates the transition detected, ordered by isotopolog and frequency.

Detections are presented in Table 7. A total of 20 stars with detections of some of the above-mentioned 27 thermal lines are included. In all cases, spectra have been smoothed to a velocity resolution of 2 km s^{-1}. Positive detections are labeled by "Y,"

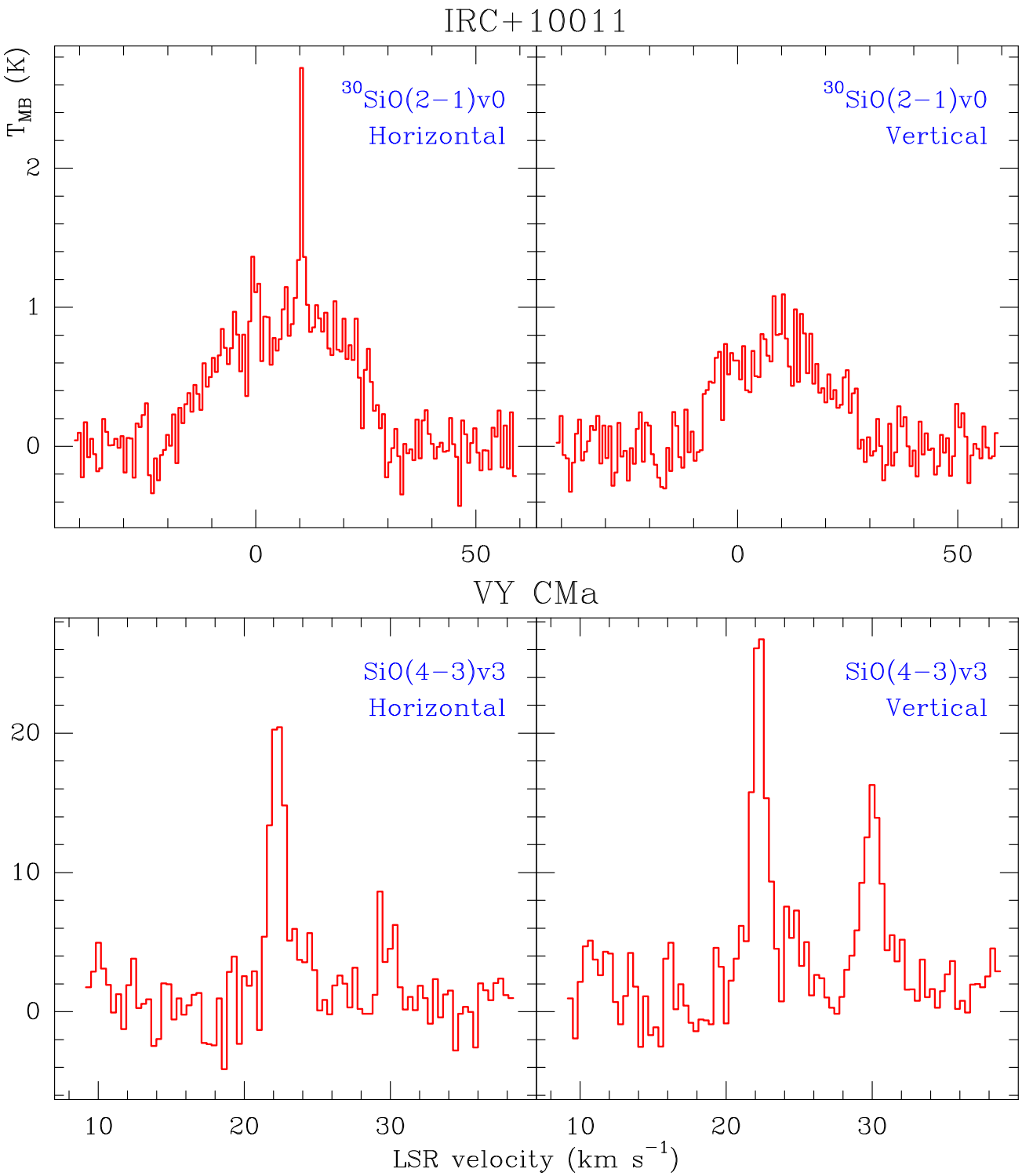

Figure 6. Two examples of highly linearly polarized velocity components. The cases shown are the ^{30}SiO $J = 2 \rightarrow 1$, $v = 0$ line toward IRC+10011 and the ^{28}SiO $J = 4 \rightarrow 3$, $v = 3$ line toward VY CMa.

negative results by "N," and detections after further smoothing by "S."

A brief analysis of the results are presented in Section 4 below.

4. Discussion

4.1. The Highest Vibrationally Excited Lines

R Cas is one of the strongest SiO maser emitters and has been the subject of numerous single-dish and interferometric observations up to $v = 3$ (see, for example, Phillips et al. 2001, 2003; McIntosh & Hayes 2008; McIntosh & Patriat 2010; Assaf et al. 2011, 2013). We report here the first tentative detection of a $v = 6$ line, corresponding to the rotational transition $J = 4 \rightarrow 3$. The line, displayed in Figure 7 (left panel), is very narrow and has been significantly detected after averaging the two linear polarizations (Table 5).

We also report the tentative detection of another $v = 6$ line, the one corresponding to the $J = 2 \rightarrow 1$ line in χ Cyg (ID 348

Table 6
Other Molecular Lines: Identification

Species and Line ID	Molecule	Transition	Frequency (MHz)	E_u (K)
A1	HCO^+	1–0	89188.5247	4.3
B1	HNC	1–0	90663.5680	4.4
C1	HCN	1–0	88631.6023	4.3
C2	$H^{13}CN$	1–0	86339.9214	4.2
C3	$H^{13}CN$	2–1	172677.8512	12.4
D1	SiS	5–4	90771.5643	13.1
D2	SiS	7–6	127076.1860	24.4
D3	^{29}SiS	5–4	89103.7489	12.8
D4	^{29}SiS	12–11	213816.1396	66.7
D5	$Si^{34}S$	5–4	88285.8282	12.7
E1	H_2S	$1_{1,0}$–$1_{0,1}$	168762.7624	27.9
E2	H_2S	$2_{2,0}$–$2_{1,1}$	216710.4365	84.0
E3	$H_2^{34}S$	$1_{1,0}$–$1_{0,1}$	167910.5160	27.8
F1	SO	2_2–1_1	86093.9500	19.3
F2	SO	3_3–2_2	129138.9230	25.5
F3	SO	4_4–3_3	172181.4600	33.8
F4	SO	5_5–4_4	215220.6530	44.1
F5	^{34}SO	6_5–5_4	215839.4361	34.4
G1	SO_2	$8_{1,7}$–$8_{0,8}$	83688.0930	36.7
G2	SO_2	$12_{2,10}$–$12_{1,11}$	128605.1300	82.6
G3	SO_2	$12_{1,11}$–$11_{2,10}$	129105.8300	76.4
G4	SO_2	$10_{2,8}$–$10_{1,9}$	129514.8100	60.9
G5	SO_2	$16_{3,13}$–$16_{2,14}$	214689.3800	147.8
H1	NaCl	10–9	130223.6270	34.4
H2	NaCl	13–12	169257.2052	56.9
H3	$Na^{37}Cl$	7–6	89220.1148	17.1
H4	$Na^{37}Cl$	17–16	216531.3010	93.4

Note. C1 line (HCN $J = 1 \rightarrow 0$) is composed of three hyperfine components; the quoted frequency corresponds to the most intense one.

in Table 4). The line, very narrow, is also depicted in Figure 7 (right panel). χ Cyg also displays the only $v = 5$ line of the whole survey. This also corresponds to the $J = 2 \rightarrow 1$ line (ID 345 in Table 4). The $J = 2 \rightarrow 1$ lines have been observed on almost consecutive days (August 1, 2, and 4; scans from 345 to 350), and both highly vibrationally excited lines have been detected in only one scan. Taking into account that both lines are detected at $\approx 3\sigma$ level, χ Cyg deserves further observations, because both highly vibrationally excited lines may be polarized and rapidly variable, as has been suggested by recent observations of the intense $J = 2 \rightarrow 1$, $v = 1$ line (Gómez-Garrido et al. 2020).

In χ Cyg, the intraday variability claimed by Gómez-Garrido et al. (2020) is confirmed by our data in the $v = 1$ and $v = 2$, $J = 2 \rightarrow 1$ lines. The HCN $J = 1 \rightarrow 0$ line, included in the same six scans as the $J = 2 \rightarrow 1$ SiO lines, does not vary by more than 3%, while the $v = 1$ and $v = 2$ line fluxes are very dispersed around the mean value, with departures from the average of up to 20%. This is clearly illustrated in Figure 8, where the integrated fluxes of the three lines are plotted as a function of the scan IDs; the fluxes are integrated between -5 and $+25$ km s^{-1} and normalized to the average of the six scans (345 to 350).

To our knowledge, there is only one reported detection of a $v = 5$ line, which is that corresponding to $J = 8 \rightarrow 7$ in VY CMa (Kamiński et al. 2013), using the SMA interferometer.

The $J = 11 \rightarrow 10$, $v = 4$ line has been reported in the high-mass young stellar object Orion Source I (Hirota et al. 2018; Kim et al. 2019). In an evolved star, however, there is only one detection of a $v = 4$ line SiO maser: the $J = 5 \rightarrow 4$ line in VY CMa (Cernicharo et al. 1993). We detected the vibrationally excited $J = 3 \rightarrow 2$ $v = 4$ line in VY CMa and for the first time in the other four sources: IRC+10011, R Leo, VX Sgr, and S Per. As expected, the line is very narrow and highly polarized, with VY CMa the only source where the line was detected in both linear polarizations; the significant detection in S Per was reached after averaging both polarizations. The narrowness of the lines is not unusual, but the significance of the detections should be monitored carefully. It is worth noting that the maser emission of this line was predicted by Herpin & Baudry (2000) as the result of infrared line overlaps.

4.2. About the Emitting Region

Masers require different physical conditions to invert the level population. It is therefore expected that the emitting volumes change from one maser to another. This is confirmed by interferometry at low v states (e. g. Gonidakis et al. 2010; Kamiński et al. 2013; Richter et al. 2013). Such restrictive physical conditions are met through different mechanisms (radiative pumping, collisional pumping, overlaps), as explained in Section 1. In addition, we are dealing with pulsating stars, which adds the time dependency of such conditions.

As our survey contains almost simultaneous observations of all masers, it is particularly suitable to get an idea about the overall distribution of the emitting regions. A first approach is provided in Figure 9, where we plot the normalized cumulative frequencies of the vibrational levels 0 to 3, as a function of the velocity range of emission. As v increases, the lines are more concentrated to smaller velocity ranges. Assuming that the velocity dispersion is correlated with the emitting volume, this tendency strongly suggests that the emitting region is confined to smaller volumes for larger v. As expected, this result also indicates that the physical conditions (temperature and density, IR radiative field) to produce maser emission become more restrictive as v increases.

Yun & Park (2012) simulated SiO maser emission in Mira-type stars under non-LTE conditions, considering different velocity gradients, and covering a complete pulsation cycle. One of the most robust results is the prediction of the $J = 1 \rightarrow 0$, $v = 2$ line being more intense than the corresponding $v = 1$ in half of the pulsation cycle, and the opposite in the other half. We can test this prediction with our sample, because a reasonably high number of stars have been observed with co-occurrence of both lines.

Our data contain a total of 150 detections of both lines (75 each) corresponding to 38 stars, and the other 4 cases: 2 with detections of the $v = 1$ line and the other 2 with detections of the $v = 2$ line. Figure 10 sketches the main findings. In the left panel, Figure 10(a), we plot the flux ratio of the $v = 2$ to $v = 1$ lines as a function of the scan ID, while in the right panel, Figure 10(b), the distribution of the same line ratio in bins of 0.2 width is shown. The median (0.84) and mean (0.11) of the sample are also indicated in the figure, which helps in inferring

Table 7
Other Molecular Lines: Detections

Source	Line																										
	A1	B1	C1	C2	C3	D1	D2	D3	D4	D5	E1	E2	E3	F1	F2	F3	F4	F5	G1	G2	G3	G4	G5	H1	H2	H3	H4
IRC+10011	Y	N	Y	Y	S	Y	Y	S	S	Y	Y	N	S	Y	Y	N	S	N	Y	N	N	Y	N	N	N	N	N
S Cas	N	N	Y	S	S	S	S	N	…	N	…	…	…	N	N	N	…	…	N	N	N	N	…	N	…	N	…
O Cet	Y	N	N	N	N	N	N	N	N	N	N	N	N	N	N	N	N	N	N	N	N	N	N	N	N	N	N
S Per	N	N	Y	N	N	N	N	N	N	N	N	N	N	N	N	N	N	N	N	N	N	N	N	N	N	N	N
NML Tau	Y	Y	Y	Y	Y	Y	Y	S	N	S	Y	N	S	Y	Y	Y	Y	N	Y	Y	Y	Y	N	N	N	N	N
TX Cam	Y	Y	Y	Y	S	Y	Y	N	N	Y	Y	N	N	Y	Y	N	N	N	Y	N	N	N	N	N	N	N	N
IRC+60154	N	N	Y	N	N	N	N	N	…	N	…	…	…	N	N	N	…	…	N	N	N	N	…	N	…	N	…
HK Ori	N	N	Y	N	N	N	…	N	…	N	…	…	…	N	…	N	…	…	N	…	…	…	…	…	…	N	…
VY CMa	Y	N	Y	Y	N	Y	Y	N	N	N	N	N	N	Y	Y	S[a]	Y	N	Y	Y[b]	S	Y	S	N	N	N	N
R Leo	N	N	Y	N	N	N	N	N	N	N	N	N	N	Y	Y	N	Y	N	N	N	N	N	N	N	N	N	N
RX Boo	N	N	Y	N	N	N	N	N	N	N	N	N	N	Y	Y	Y	S	N	Y	N	S	Y	N	N	N	N	N
U Her	N	N	Y	N	N	N	N	N	…	N	…	…	…	N	S	N	…	…	N	N	N	N	…	N	…	N	…
VX Sgr	Y	N	Y	N	N	S	S	N	N	N	…	N	…	S	Y	S	Y	N	S	Y	N	S	N	N	…	N	N
V1111 Oph	Y	N	Y	Y	N	Y	Y	N	N	N	…	N	…	S	S	N	Y	N	Y	N	N	S	N	N	…	N	N
R Aql	N	N	Y	N	N	N	N	N	…	N	…	…	…	Y	Y	S	…	…	Y	N	Y	Y	…	N	…	N	…
χ Cyg	N	N	Y	Y	Y	N	N	N	N	N	N	N	N	N	N	N	N	N	N	N	N	N	N	N	N	N	N
RR Aql	N	N	Y	N	N	N	N	N	…	N	…	…	…	N	S	S	…	…	Y	S	S	S	…	N	…	N	…
NML Cyg	Y	S	Y	Y	S	Y	Y	N	N	N	Y	Y	Y	Y	Y	Y	Y	S	Y	Y	Y	Y	S	Y	Y	Y	S
μ Cep	Y	N	Y	N	N	N	N	N	N	N	N	N	N	Y	N	N	N	N	N	N	N	N	N	N	N	N	N
R Cas	Y	N	Y	Y	N	N	N	N	N	N	N	N	N	Y	Y	Y	Y	N	Y	S	Y	Y	N	N	N	N	N

Notes. All spectra have been averaged and smoothed down to $\approx$2 km s^{-1}. Y: detected. N: not detected. S: detected after smoothing worse than 2 km s^{-1}.
[a] Instrumental problems close in frequency, but clear detection.
[b] Blended with ^{29}SiO(3–2) $v = 0$.

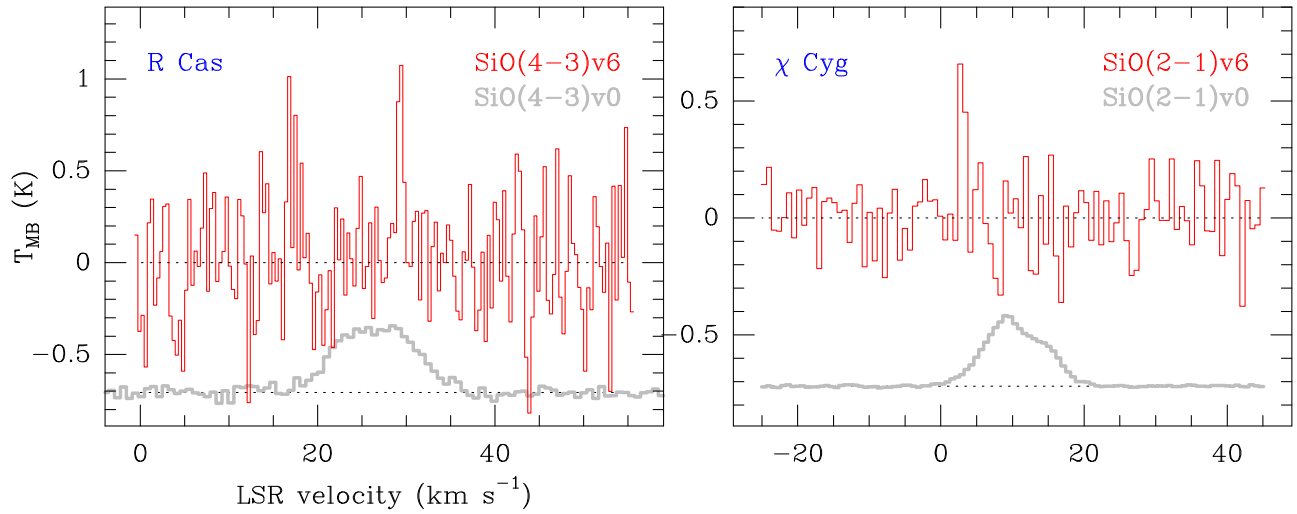

Figure 7. First tentative detections of $v = 6$ SiO maser lines. They correspond to R Cas ($J = 4 \rightarrow 3$; left panel) and χ Cyg ($J = 2 \rightarrow 1$; right panel). Both $v = 6$ lines are very narrow and displayed in red. To visualize the velocity range of emission of the other SiO lines, the corresponding $v = 0$ line (not to scale) is displayed in gray.

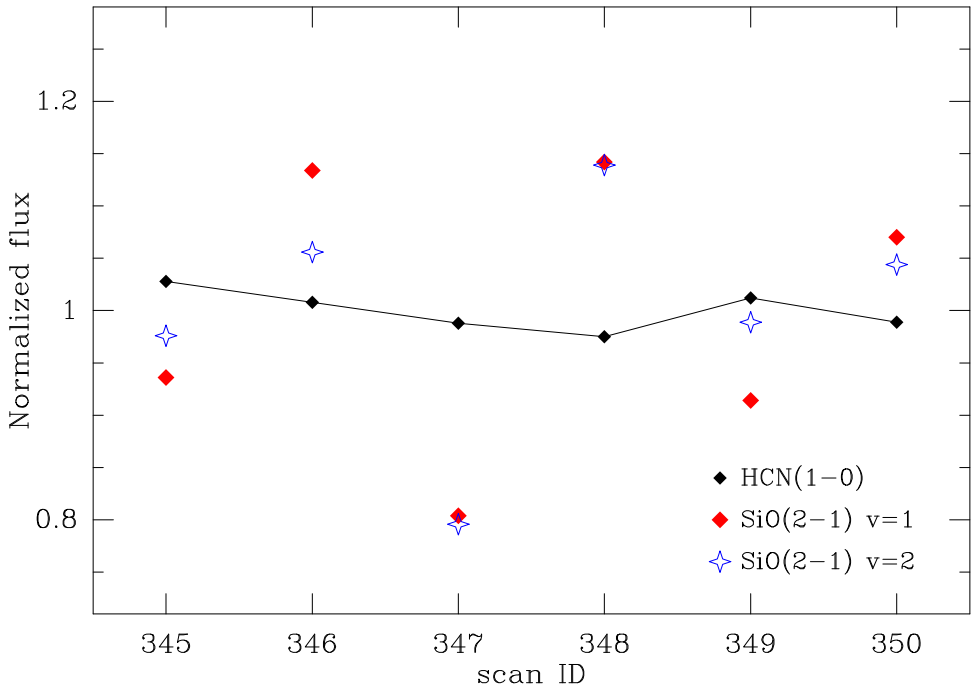

Figure 8. Intraday variability of χ Cyg. Fluxes of the thermal HCN $J = 1 \rightarrow 0$ and $J = 2 \rightarrow 1$, $v = 1, 2$ of the SiO lines are plotted as a function of their scans IDs. To facilitate the comparison, fluxes (computed from -5 to $+25$ km s^{-1}) are normalized to their respective average values. Scan IDs are explained in Table 2, and correspond to both linear polarizations observed during August 1, 2, and 4. Note that the HCN normalized flux (black marks) remains well within $\pm 3\%$, while the SiO line fluxes (blue and red marks) change significantly (up to 20%). This demonstrates the high polarization and rapid variability of the SiO lines in this source.

a rather uniform distribution of the ratios around values close to 1, i.e., without a clear dominance of one line over the other.

We have counted a total of 33 sources (44%), where $F(v = 2)$ is greater than $F(v = 1)$, and 42 cases (56%) with the opposite behavior. The overall results of this rather simple analysis seem to confirm the prediction made by Yun & Park (2012), although a more thorough and case-by-case analysis should be performed to provide a firm confirmation.

4.3. "Bonus" Thermal Lines

In order to provide an overall view of the thermal lines detected, we divided them into four groups. The first group is constituted by the C-bearing molecules HCO^+, HNC, HCN, and $H^{13}CN$. HCO^+ (A1 in Table 6) is a widespread molecule aside from H_2 and CO, abundant in a variety of astronomical sources such as comets, diffuse clouds, and molecular clouds, but with abundances below the predicted values in AGB stars (Glassgold 1996). HCO^+ was first discovered in VY CMa (Ziurys et al. 2007) and later in other sources (e.g., Pulliam et al. 2011), including TX Cam and NML Cyg. We detect HCO^+ in 10 sources.

HNC (B1 in Table 6) was first tentatively reported by Lindqvist et al. (1988) in TX Cam, and later detected by Ziurys et al. (2009) in VY CMa. We detect HNC in TX Cam, NML Tau, and NML Cyg, but not in VY CMa probably due to a high noise level. HCN (C1 in Table 6) is the most common molecule found in the survey, detected in 19 out of the 20

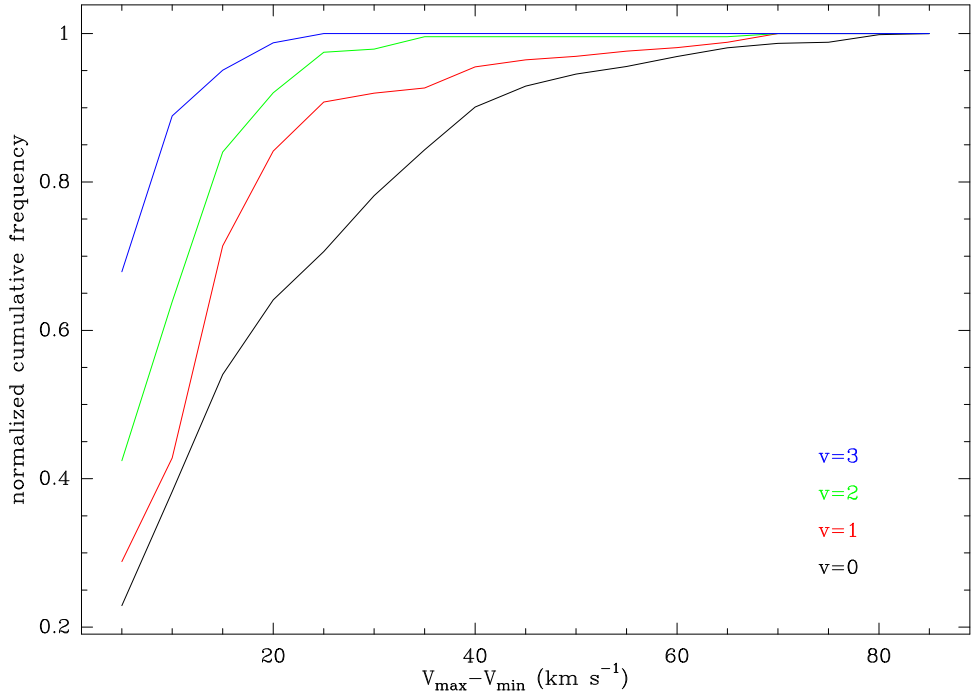

Figure 9. Normalized cumulative frequencies of the different vibrational levels for the whole sample, as a function of the velocity range of emission.

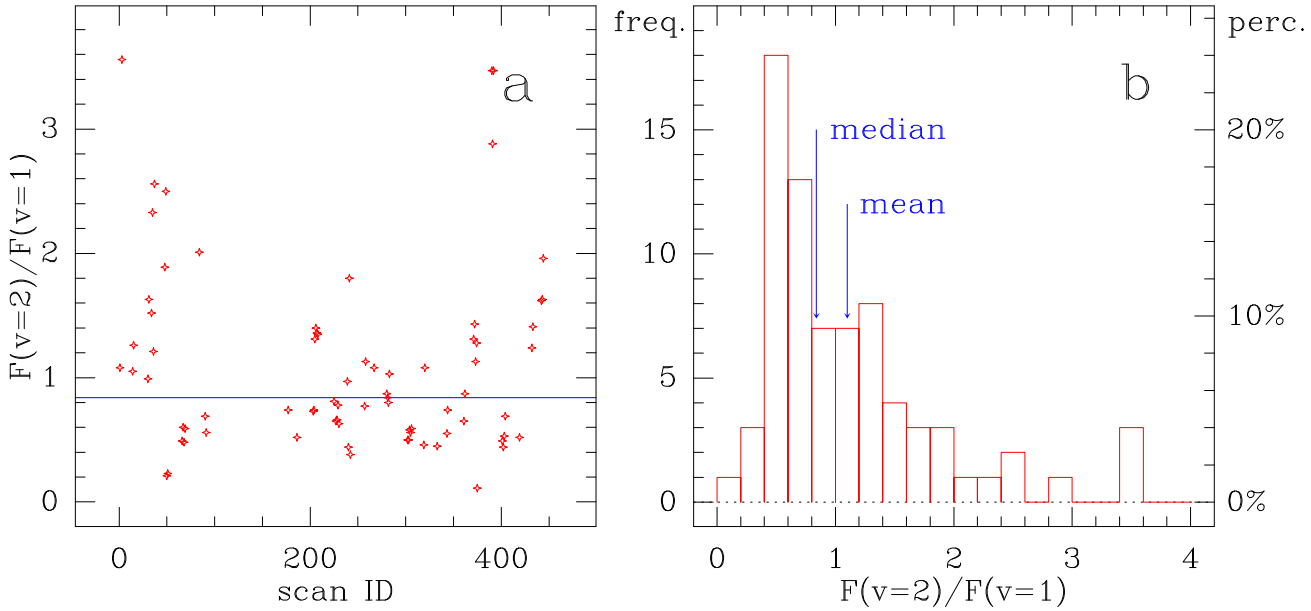

Figure 10. Relative intensities of the $J = 1 \rightarrow 0$, $v = 1$ and $v = 2$ lines. (a) Flux ratios $v = 2/v = 1$ plotted as a function of the scan ID; the blue line indicates the median of the sample. (b) Distribution of the same ratios, expressed in absolute (left axis) and relative (right axis) frequencies; the median (0.84) and the mean (0.11) of the sample are also plotted as blue arrows.

sources. It was already detected by several authors (e.g., Lindqvist et al. 1988; Nercessian et al. 1989; Ziurys et al. 2009) in some of the stars of our sample (IRC+10011, NML Tau, TX Cam, VY CMa, VX Sgr, NML Cyg, and R Cas). Its isotopolog $H^{13}CN$ (C2 and C3 in Table 6) is less abundant and therefore hardly detected; it was reported and analyzed in IRC+10011, NML Tau (=IK Tau), VY CMa, and NML Cyg (Nercessian et al. 1989; Tenenbaum et al. 2010a; Velilla Prieto et al. 2017).

The second group (lines D and E in Table 6) constitutes the sulfur-bearing molecules SiS and H_2S, and some of their isotopologs. Around evolved stars, SiS and H_2S are tracers of warm gas, probably above 100 K (Sánchez Contreras et al. 2015, and references therein), and are good tracers of the dust formation zones (Cernicharo et al. 2011). SiS was first reported by Lindqvist et al. (1988) in TX Cam, and later in NML Tau (Bujarrabal et al. 1994); we confirm here those detections and add other six to the list: IRC+10011, S Cas, VY CMa, VX Sgr, V111 Oph, and NML Cyg.

H_2S was firmly detected by Omont et al. (1993) in IRC +10011, NML Tau, VY CMa, and NML Cyg; a tentative detection was also reported by Danilovich et al. (2017) in V1111 Oph. We add here the detection of H_2S in TX Cam.

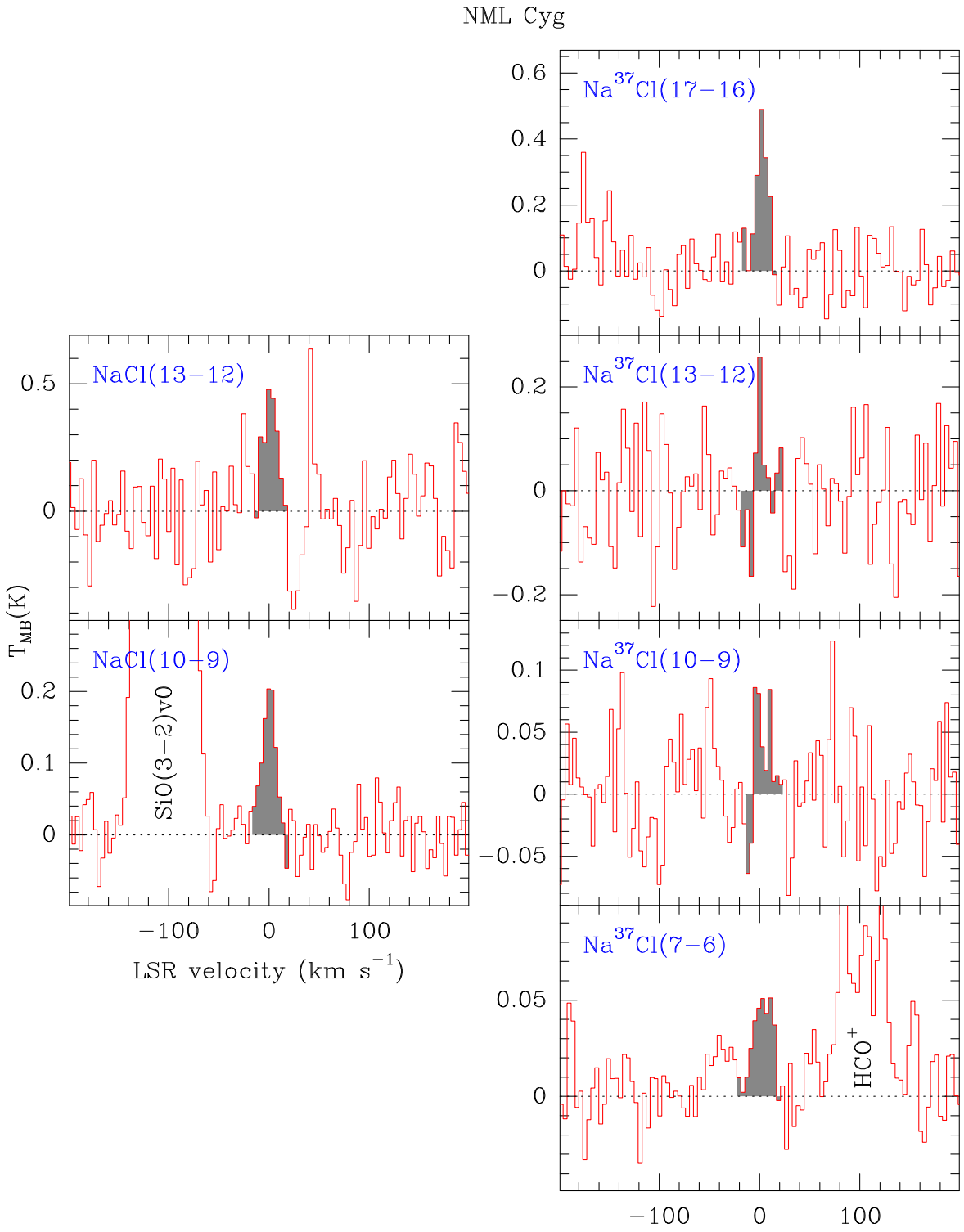

Figure 11. NaCl and $Na^{37}Cl$ lines in NML Cyg. Transitions are indicated at the top left of each panel. Lines are shaded in the velocity range of emission of other lines in this source. Two other close lines (HCO^+ and SiO) fall inside the plot, as indicated.

The third group (lines F and G in Table 6) is formed by sulfur oxides. Together with the SiO maser lines, sulfur oxides are the most abundant molecules in oxygen-rich CSEs. SO (F1 to F5 lines in Table 6) and SO_2 (G1 to G5 in the same table) have been detected since the first molecular studies of these sources. Omont et al. (1993) detected up to three lines of SO_2 in IRC+10011, NML Tau, VY CMa, RX Boo, and NML Cyg, none of them coincident with those reported in our survey. Later, Tenenbaum et al. (2010a) performed a sensitive survey of VY CMa at 1 mm and reported several S-bearing molecules in this source. A similar spectral survey toward NML Tau, but with a high spectral coverage (from 79 to 356 GHz), was recently published (Velilla Prieto et al. 2017) with similar findings. We detected SO and SO_2 in the same sources as in the Omont et al. (1993) article, and also in VX Sgr and R Cas. The less-abundant isotopolog ^{34}SO (line F5) is detected only in

NML Cyg. The $16_{3,13}-16_{2,14}$ line of SO_2 (G5), with the highest upper energy level (147.8 K) is only detected in VY Cma and NML Cyg.

The fourth group is constituted by NaCl and its isotopolog $Na^{37}Cl$. Four lines have been clearly identified, labeled as H1 to H4 in Table 6. Since the first identification in CSEs (Cernicharo & Guelin 1987), this metal refractory molecule has been firmly observed in IK Tau and VY CMa (Milam et al. 2007; Tenenbaum et al. 2010b; Kamiński et al. 2013; Decin et al. 2016; Velilla Prieto et al. 2017); recently, it was tentatively detected in R Dor (De Beck & Olofsson 2018), although not confirmed with ALMA data (Decin et al. 2018). We failed to detect NaCl in IK Tau and VY CMa, although report the first detection in NML Cyg, as shown in Figure 11. Besides the lines quoted in Table 7, the observed frequencies also include the $J = 10 \rightarrow 9$ and $13 \rightarrow 12$ lines of $Na^{37}Cl$ (also shown in Figure 11), not detected probably due to insufficient noise level.

5. Conclusions

This work reports the results of a nearly complete survey of SiO, ^{29}SiO, and ^{30}SiO emission for $J = 1 \rightarrow 0$ to $5 \rightarrow 4$, in 67 oxygen-rich stars. The stars have been chosen to span a large range of mass-loss rates, from 10^{-8} up to 10^{-4} $M_{\odot}$ yr^{-1}. In all rotational transitions, we surveyed simultaneously the vibrational levels v from 0 to 6, completing a list of 61 maser lines. A total of 1474 detections is reported.

The observations were made in a relatively short time (weeks for the $J = 1 \rightarrow 0$ and four days for the others); therefore, we can consider that most stages of the pulsation phases were randomly tested.

As expected, several maser lines exhibit significant variability and are highly linearly or circularly polarized. The most prominent cases have been highlighted (Section 3.2, Figures 5 and 6).

Several lines are reported for the first time. The first detection of a $v = 6$ line in R Cas and χ Cyg is remarkable. χ Cyg also displays the only $v = 5$ line detected. The $v = 4$ vibrational state only depicts rotational lines in the $J = 3 \rightarrow 2$ transition; very narrow and highly polarized, this line was detected in VY CMa and for the first time in IRC+10011, R Leo, VX Sgr, and S Per.

As a by-product, we also report the detection of other 27 thermal lines over a total of 20 sources. The lines correspond to common density tracers (like HCO^+ and HCN), refractory molecules (like SiS), S-bearing molecules (H_2S, SO, SO_2), and the less observed NaCl, detected for the first time in NML Cyg (Figure 11).

SiO plays a key role in the process of dust formation under the appropriate physical conditions. The database generated by this survey would be the basis of the ambitious modeling of SiO maser emission and the overall evolution of the circumstellar envelopes.

This work was partially done under the Host Country Radio Astronomy program at MDSCC. The authors wish to thank the MDSCC and IRAM staff for their kind and professional support during the observations. J.R.R. acknowledges the support from projects ESP2017-86582-C4-1-R and PID2019-105552RB-C41 (Ministerio de Ciencia e Innovación). J.C. thanks ERC for Synergy grant ERC-2013-Syg-610256-NANOCOSMOS.

Facilities: MDSCC:DSS-54, IRAM:30 m.

ORCID iDs

J. R. Rizzo https://orcid.org/0000-0002-8443-6631
J. Cernicharo https://orcid.org/0000-0002-3518-2524

References

Alcolea, J., & Bujarrabal, V. 1992, A&A, 253, 475
Assaf, K. A., Diamond, P. J., Richards, A. M. S., et al. 2011, MNRAS, 415, 1083
Assaf, K. A., Diamond, P. J., Richards, A. M. S., et al. 2013, MNRAS, 431, 1077
Balança, C., & Dayou, F. 2017, MNRAS, 469, 1673
Bujarrabal, V. 1994a, A&A, 285, 953
Bujarrabal, V. 1994b, A&A, 285, 971
Bujarrabal, V., Alcolea, J., Sánchez Contreras, C., & Colomer, F. 1996, A&A, 314, 883
Bujarrabal, V., Fuente, A., & Omont, A. 1994, A&A, 285, 247
Carter, M., Lazareff, B., Maier, D., et al. 2012, A&A, 538, A89
Cernicharo, J. 2012, in EAS Publications Ser. 58, European Conf. on Laboratory Astrophysics, ed. C. Stehlé et al. (Les Ulis: EDP Sciences), 251
Cernicharo, J., Agúndez, M., & Guélin, M. 2011, in IAU Symp. 280, The Molecular Universe, ed. J. Cernicharo & R. Bachiller (Cambridge: Cambridge Univ. Press), 237
Cernicharo, J., & Bujarrabal, V. 1992, ApJL, 401, L109
Cernicharo, J., Bujarrabal, V., & Lucas, R. 1991, A&A, 249, L27
Cernicharo, J., Bujarrabal, V., & Santarén, J. L. 1993, ApJL, 407, L33
Cernicharo, J., & Guelin, M. 1987, A&A, 183, L10
Cho, S.-H., Kaifu, N., & Ukita, N. 1996, A&AS, 115, 117
Danilovich, T., Van de Sande, M., De Beck, E., et al. 2017, A&A, 606, A124
Dayou, F., & Balança, C. 2006, A&A, 459, 297
De Beck, E., & Olofsson, H. 2018, A&A, 615, A8
Decin, L., Richards, A. M. S., Danilovich, T., et al. 2018, A&A, 615, A28
Decin, L., Richards, A. M. S., Millar, T. J., et al. 2016, A&A, 592, A76
Deguchi, S., Good, J., Fan, Y., et al. 1983, ApJL, 264, L65
Glassgold, A. E. 1996, ARA&A, 34, 241
Gómez-Garrido, M., Bujarrabal, V., Alcolea, J., et al. 2020, A&A, 642, A213
Gonidakis, I., Diamond, P. J., & Kemball, A. J. 2010, MNRAS, 406, 395
González-Alfonso, E., Alcolea, J., & Cernicharo, J. 1996, A&A, 313, L13
González-Alfonso, E., & Cernicharo, J. 1997, A&A, 322, 938
Gray, M. D., Ivison, R. J., Yates, J. A., et al. 1995, MNRAS, 277, L67
Gray, M. D., Wittkowski, M., Scholz, M., et al. 2009, MNRAS, 394, 51
Herpin, F., & Baudry, A. 2000, A&A, 359, 1117
Hirota, T., Machida, M. N., Matsushita, Y., et al. 2018, in IAU Symp. 336, Astrophysical Masers: Unlocking the Mysteries of the Universe, ed. A. Tarik et al. (Cambridge: Cambridge Univ. Press), 207
Humphreys, E. M. L., Gray, M. D., Yates, J. A., et al. 2002, A&A, 386, 256
Jewell, P. R., Dickinson, D. F., Snyder, L. E., & Clemens, D. P. 1987, ApJ, 323, 749
Kamiński, T., Gottlieb, C. A., Young, K. H., et al. 2013, ApJS, 209, 38
Kim, J., Cho, S.-H., Oh, C. S., & Byun, D.-Y. 2010, ApJS, 188, 209
Kim, M. K., Hirota, T., Machida, M. N., et al. 2019, ApJ, 872, 64
Klein, B., Krämer, I., Hochgürtel, S., et al. 2009, in Proc. Twentieth Int. Symp. on Space Terahertz Technology, ed. E. Bryerton et al., 199
Langer, S. H., & Watson, W. D. 1984, ApJ, 284, 751
Lindqvist, M., Nyman, L.-A., Olofsson, H., et al. 1988, A&A, 205, L15
Mauersberger, R., Guelin, M., Martín-Pintado, J., et al. 1989, A&AS, 79, 217
McIntosh, G. C., & Hayes, A. M. 2008, ApJ, 678, 1324
McIntosh, G. C., & Patriat, R. 2010, PASP, 122, 1187
Milam, S. N., Apponi, A. J., Woolf, N. J., et al. 2007, ApJL, 668, L131
Müller, H. S. P., Schlöder, F., Stutzki, J., & Winnewisser, G. 2005, JMoSt, 742, 215
Müller, H. S. P., Thorwirth, S., Roth, D. A., & Winnewisser, G. 2001, A&A, 370, L49
Nercessian, E., Omont, A., Benayoun, J. J., & Guilloteau, S. 1989, A&A, 210, 225
Olofsson, H., Rydbeck, O. E. H., Lane, A. P., & Predmore, C. R. 1981, ApJL, 247, L81
Olofsson, H., Rydbeck, O. E. H., & Nyman, L.-A. 1985, A&A, 150, 169
Omont, A., Lucas, R., Morris, M., et al. 1993, A&A, 267, 490
Pardo, J. R., Alcolea, J., Bujarrabal, V., et al. 2004, A&A, 424, 145
Pardo, J. R., Cernicharo, J., González-Alfonso, E., & Bujarrabal, V. 1998, A&A, 329, 219

Pardo, J. R., Cernicharo, J., & Serabyn, E. 2001, ITAP, 49, 12
Phillips, R. B., Sivakoff, G. R., Lonsdale, C. J., et al. 2001, AJ, 122, 2679
Phillips, R. B., Straughn, A. H., Doeleman, S. S., et al. 2003, ApJL, 588, L105
Pickett, H. M., Poynter, R. L., Cohen, E. A., et al. 1998, JQSRT, 60, 883
Pulliam, R. L., Edwards, J. L., & Ziurys, L. M. 2011, ApJ, 743, 36
Rausch, E., Kegel, W. H., Tsuji, T., & Piehler, G. 1996, A&A, 315, 533
Richter, L., Kemball, A., & Jonas, J. 2013, MNRAS, 436, 1708
Rizzo, J. R., & García-Miró, G. 2013, in Proc. of the Scientific Meeting of the Spanish Astronomical Society 10, Highlights of Spanish Astrophysics 7, ed. J. C. Guirado et al., 904
Rizzo, J. R., Pedreira, A., Gutiérrez Bustos, M., et al. 2012, A&A, 542, A63
Sánchez Contreras, C., Velilla Prieto, L., Agúndez, M., et al. 2015, A&A, 577, A52
Schwartz, P. R., Zuckerman, B., & Bologna, J. M. 1982, ApJL, 256, L55
Shinnaga, H., Claussen, M. J., Yamamoto, S., & Shimojo, M. 2017, PASJ, 69, L10
Shinnaga, H., Moran, J. M., Young, K. H., & Ho, P. T. P. 2004, ApJL, 616, L47
Soria-Ruiz, R., Alcolea, J., Colomer, F., et al. 2007, A&A, 468, L1
Tenenbaum, E. D., Dodd, J. L., Milam, S. N., et al. 2010a, ApJL, 720, L102
Tenenbaum, E. D., Dodd, J. L., Milam, S. N., et al. 2010b, ApJS, 190, 348
Velilla Prieto, L., Sánchez Contreras, C., Cernicharo, J., et al. 2017, A&A, 597, A25
Vlemmings, W. H. T., Humphreys, E. M. L., & Franco-Hernández, R. 2011, ApJ, 728, 149
Wittkowski, M., Boboltz, D. A., Ohnaka, K., et al. 2007, A&A, 470, 191
Yun, Y. J., & Park, Y.-S. 2012, A&A, 545, A136
Ziurys, L. M., Milam, S. N., Apponi, A. J., & Woolf, N. J. 2007, Natur, 447, 1094
Ziurys, L. M., Tenenbaum, E. D., Pulliam, R. L., Woolf, N. J., & Milam, S. N. 2009, ApJ, 695, 1604